GeroScience (2023) 45:2851–2872
https://doi.org/10.1007/s11357-023-00839-w

ORIGINAL ARTICLE

Imaging the time course, morphology, neuronal tissue compression, and resolution of cerebral microhemorrhages in mice using intravital two-photon microscopy: insights into arteriolar, capillary, and venular origin

Janet Faakye · Ádám Nyúl-Tóth · Rafal Gulej · Boglarka Csik · Stefano Tarantini · Santny Shanmugarama · Calin Prodan · Peter Mukli · Andriy Yabluchanskiy · Shannon Conley · Peter Toth · Anna Csiszar · Zoltan Ungvari

Received: 19 March 2023 / Accepted: 24 May 2023 / Published online: 20 June 2023

Abstract Cerebral microhemorrhages (CMHs, microbleeds), a manifestation of age-related cerebral small vessel disease, contribute to the pathogenesis of cognitive decline and dementia in older adults. Histological studies have revealed that CMHs exhibit distinct morphologies, which may be attributed to differences in intravascular pressure and the size of the vessels of origin. Our study aimed to establish a direct relationship between the size/morphology of CMHs and the size/anatomy of the microvessel of origin. To achieve this goal, we adapted and optimized intravital two-photon microscopy-based imaging methods to monitor the development of CMHs in mice equipped with a chronic cranial window upon high-energy laser light-induced photodisruption of a targeted cortical arteriole, capillary, or venule. We assessed the time course of extravasation of fluorescently labeled blood and determined the morphology and size/volume of the induced CMHs. Our findings reveal striking similarities between the bleed morphologies observed in hypertension-induced CMHs in models of aging and those originating from different targeted vessels via multiphoton laser ablation. Arteriolar bleeds, which are larger (> 100 μm) and more widely dispersed,

Janet Faakye and Ádám Nyúl-Tóth have equal contributions.

J. Faakye · Á. Nyúl-Tóth (✉) · R. Gulej · B. Csik · S. Tarantini · S. Shanmugarama · P. Mukli · A. Yabluchanskiy · P. Toth · A. Csiszar · Z. Ungvari (✉)
Vascular Cognitive Impairment, Neurodegeneration, and Healthy Brain Aging Program, Department of Neurosurgery, University of Oklahoma Health Sciences Center, Oklahoma City, OK, USA
e-mail: adam-nyultoth@ouhsc.edu

Z. Ungvari
e-mail: zoltan-ungvari@ouhsc.edu

J. Faakye · Á. Nyúl-Tóth · R. Gulej · B. Csik · S. Tarantini · S. Shanmugarama · P. Mukli · A. Yabluchanskiy · S. Conley · P. Toth · A. Csiszar · Z. Ungvari
Oklahoma Center for Geroscience and Healthy Brain Aging, University of Oklahoma Health Sciences Center, Oklahoma City, OK, USA

Á. Nyúl-Tóth · R. Gulej · B. Csik · S. Tarantini · Z. Ungvari
International Training Program in Geroscience, Doctoral School of Basic and Translational Medicine/Department of Public Health, Semmelweis University, Budapest, Hungary

S. Tarantini · A. Csiszar · Z. Ungvari
Stephenson Cancer Center, University of Oklahoma, Oklahoma City, OK, USA

C. Prodan
Veterans Affairs Medical Center, Oklahoma City, OK, USA

are distinguished from venular bleeds, which are smaller and exhibit a distinct diffuse morphology. Capillary bleeds are circular and smaller (< 10 µm) in size. Our study supports the concept that CMHs can occur at any location in the vascular tree, and that each type of vessel produces microbleeds with a distinct morphology. Development of CMHs resulted in immediate constriction of capillaries, likely due to pericyte activation and constriction of precapillary arterioles. Additionally, tissue displacement observed in association with arteriolar CMHs suggests that they can affect an area with a radius of ~ 50 µm to ~ 100 µm, creating an area at risk for ischemia. Longitudinal imaging of CMHs allowed us to visualize reactive astrocytosis and bleed resolution during a 30-day period. Our study provides new insights into the development and morphology of CMHs, highlighting the potential clinical implications of differentiating between the types of vessels involved in the pathogenesis of CMHs. This information may help in the development of targeted interventions aimed at reducing the risk of cerebral small vessel disease-related cognitive decline and dementia in older adults.

Keywords Microbleed · VCID · Age-related cognitive decline · Small vessel disease · SVD

C. Prodan
Department of Neurology, University of Oklahoma Health Sciences Center, Oklahoma City, OK, USA

S. Conley
Department of Cell Biology, University of Oklahoma Health Sciences Center, Oklahoma City, OK, USA

P. Toth
Department of Neurosurgery, Medical School, University of Pecs, Pecs, Hungary

A. Csiszar
International Training Program in Geroscience, Doctoral School of Basic and Translational Medicine/Department of Translational Medicine, Semmelweis University, Budapest, Hungary

Introduction

Cerebral microhemorrhages (CMH; also described as microbleeds, multifocal signal loss lesions, petechial hemorrhages) are intracerebral bleeds, typically less than 5 mm in size, that can result from a variety of underlying conditions in older adults. CMHs are due to the rupture of vessels of the cerebral microcirculation. CMHs typically appear as small, round, or ovoid hypointense lesions on T2*-weighted Gradient-Recall Echo (T2*-GRE) or susceptibility-weighted imaging (SWI) MRI sequences. These lesions correspond to focal hemosiderin depositions, which are iron deposits that result from the breakdown of red blood cells.

Aging is a well-established risk factor for CMHs [1–11]. The prevalence of CMHs significantly increases with age, from ~ 6.5% in persons aged 45 to 50 years to ~ 50% or more in elderly patients [9, 12]. Other important risk factors include hypertension, cerebrovascular disease (individuals with a history of stroke or transient ischemic attack are at increased risk of developing CMH), and amyloid angiopathy. CMHs contribute to the progressive impairment of cognitive function in older adults with compromised cerebrovascular health [3, 8, 13–22]. Possible mechanisms for this association are that CMHs can cause damage to the brain tissue surrounding the hemorrhage, can cause tissue ischemia by blocking blood flow, and can promote neuroinflammation that adversely impacts neuronal function. They also likely impair brain connectivity, adversely affecting cognitive function and contributing to cognitive decline.

There is mounting evidence to suggest that CMHs can originate from different levels of cerebral microcirculation [9, 23]. Epidemiological studies have shown that arterial hypertension is a critical risk factor in the development of CMHs [12, 24], particularly in older adults. In the Rotterdam Scan Study [12], arterial hypertension was identified as an especially strong risk factor for CMHs (hazard ratio: 1.66). It is assumed that high arterial pressure can penetrate the cerebral microcirculation in older adults due to impaired autoregulatory myogenic protection [25–29], leading to

the formation of CMHs at the level of small arteries, arterioles, and/or capillaries [23].

Pathological evidence shows that CMHs originate frequently from capillaries in older adults even in the absence of hypertension [9]. Amyloid pathologies affecting the cerebral microcirculation (cerebral amyloid angiopathy (CAA)) are also an important risk factor for the development of CMHs [30–34]. The existing evidence suggests that CAA promotes CMHs originating from the capillaries [35].

There is also evidence from both preclinical and clinical investigations suggesting that CMHs may also originate from the cerebral venous circulation [23, 36–38], especially in pathological conditions associated with increased venous pressure [39]. In support of this concept, clinical observations suggest that increases in venous pressure due to a prolonged Valsalva maneuver may promote the development of CMHs in older adults [40]. Additionally, experimental studies show that in mouse models with jugular vein ligation, venous congestion also exacerbates the genesis of venular CMHs [41]. Aging and CAA may also promote CMHs in the venous circulation [36].

Histological studies of brains derived from mouse models of CMHs revealed that CMHs exhibit distinct morphologies [41–51]. At least three morphological CMH subtypes have been identified [41–44]. Differences in shape (round, diffuse, perivascular) and size/volume of CMHs have been attributed to differences in intravascular pressure and size of the vessels of origin [41–44]. However, there are no studies extant in which the relationship between CMH size/morphology and size/anatomy of the microvessel of origin could be directly established.

The present study was designed to test the hypothesis that rupture of arterioles result in larger spherical CMHs, whereas rupture of capillaries and venules lead to the genesis of smaller and more diffuse CMHs. To test our hypothesis, we adapted and optimized intravital two-photon microscopy-based imaging methods to monitor the development of CMHs in mice equipped with a chronic cranial window upon high-energy laser light-induced photodisruption [52] of a targeted cortical arteriole, capillary, or venule. The time course of extravasation of fluorescently labeled blood was assessed and morphology and size/volume of the induced CMHs were determined. A second motivation was to visualize the microvascular constriction elicited by the extravasated blood, the displacement of the neuronal tissue by CMH, and chronic resolution of CMHs.

Methods

Animal models

Adult (5- to 10-month-old) and aged (24-month-old) male and female C57BL/6 mice purchased from Charles River Laboratories (Wilmington, MA) were used for the induced CMH model. For visualization of microvascular constriction upon induction of CMH Myh11-Cre^{ERT2} [B6.FVB-Tg(Myh11-icre/ERT2)1Soff/J] × *ROSA* $^{f/ftdT}$ [(B6.Cg-*Gt(ROSA)26Sor*$^{tm14(CAG-tdTomato)Hze}$/J] mice were used. These animals, hereinafter designated as MYH11^{tdTomato} mice, express robust tdTomato signal in the Myh11 + mural cells of the vasculature after induction of Cre-recombinase with tamoxifen (at ~ 4 months of age), enabling the visualization of changes in vascular diameter by intravital two-photon microscopy. Animals were housed under specific pathogen-free barrier conditions in the Rodent Barrier Facility at University of Oklahoma Health Sciences Center (OUHSC) under a controlled photoperiod (12-h light; 12-h dark) with unlimited access to water and were fed a standard AIN-93G diet (ad libitum). One week before cranial window surgery, mice were transferred to the conventional animal facility of the OUHSC and single housed after surgery. All procedures were approved by the Institutional Animal Use and Care Committee of the University of Oklahoma Health Sciences Center.

Chronic cranial window surgery

Animals were equipped with a chronic cranial window as previously described [53]. In brief, animals were anesthetized with 2–3% isoflurane (ISOTHESIA, Henry Schein Animal Health, OH,

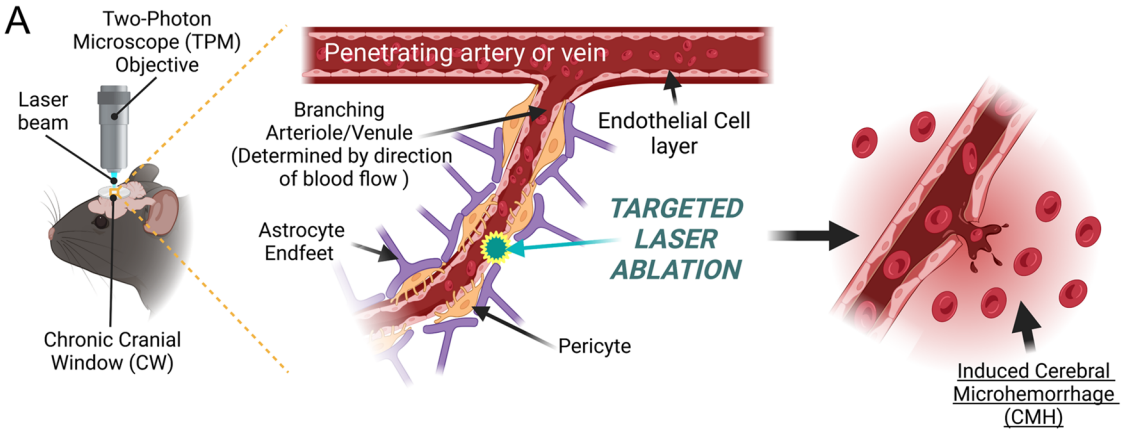
A
Two-Photon Microscope (TPM) Objective
Laser beam
Chronic Cranial Window (CW)
Penetrating artery or vein
Branching Arteriole/Venule (Determined by direction of blood flow)
Endothelial Cell layer
Astrocyte Endfeet
TARGETED LASER ABLATION
Pericyte
Induced Cerebral Microhemorrhage (CMH)

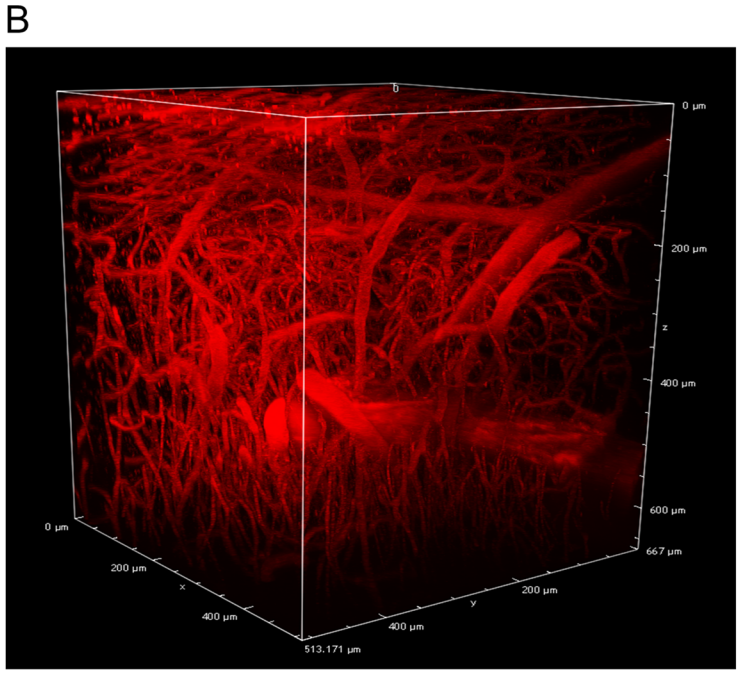
B
0 µm
200 µm
400 µm
600 µm
667 µm
513.171 µm

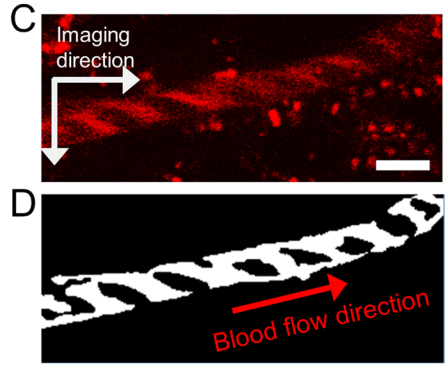
C
Imaging direction
D
Blood flow direction

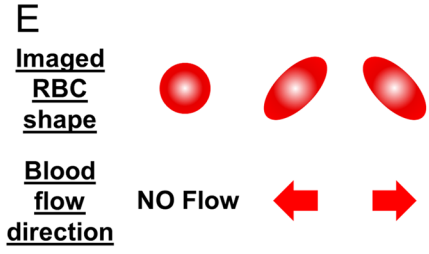
E
Imaged RBC shape
Blood flow direction
NO Flow

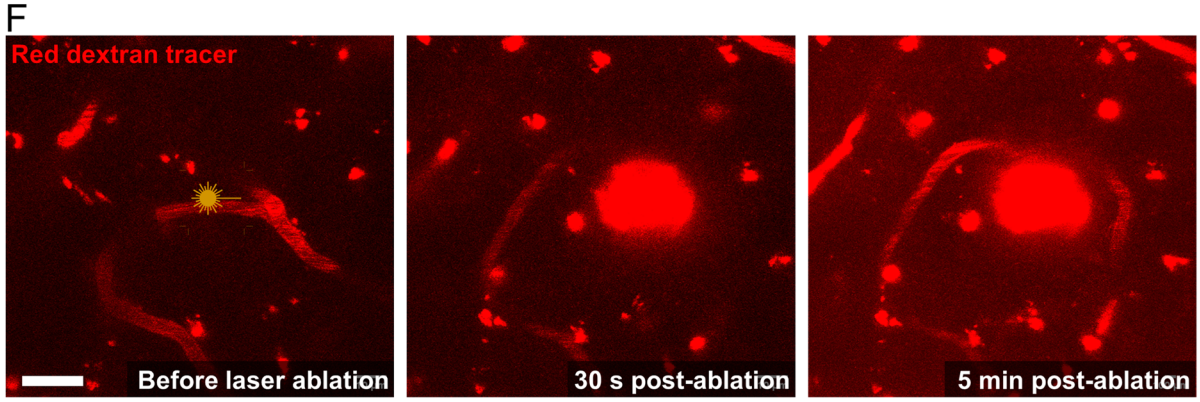
F
Red dextran tracer
Before laser ablation
30 s post-ablation
5 min post-ablation

◂**Fig. 1** Two-photon laser ablation of cerebral microvessels enables controlled microbleed formation. **A** Schematic representation of the experimental model, which includes chronic cranial window surgery and laser ablation techniques (created with BioRender). Following a recovery period after the application of a chronic cranial window, mice were subjected to intravital imaging with two-photon microscopy using a high-frequency laser for both imaging and CMH induction. High-resolution z-stacks were obtained before and after CMH induction, and the progression of CMH formation was recorded using high-magnification fast roundtrip mode to reduce the time of fluorophore bleaching and to improve temporal resolution. Induction was assessed on the edge of the targeted microvessel to avoid further ablation and complete vessel closure. **B** High-resolution 3D image of brain vasculature at a depth of approximately 600 µm, imaged through a cranial window. The image clearly shows branching arterioles. The upper ~ 50 µm regions were excluded to avoid the meningeal vessels, and CMH was induced within the brain parenchyma. **C** In vivo image of a cortical arteriole situated 100 µm below the pial surface, showing the direction of red blood cells (RBCs). Scale bar: 10 µm. **D** The thresholded image with black lines indicating RBC shadows and arrows indicating their direction. **E** A schematic explaining the link between the direction of microvascular blood flow and the shape of RBC shadows. **F** Representative two-photon images demonstrating a laser ablation-induced CMH. A brief burst of tightly focused femtosecond laser pulses was used to irradiate the vessel wall, resulting in the extravasation of blood containing Texas-Red labeled dextran. Fluorescently labeled blood plasma and RBCs were pushed into the brain. The targeted vessel was imaged 30 s and 5 min after ablation, revealing the creation of the CMH. Scale bar: 20 µm

USA) gas via inhalation with Surgivet Classic T3 vaporizer (Smiths Medical, Minneapolis, MN, USA) with 1–2 L/min flow rate before and during the surgery. Eyeblink, toe, and tail pinch reflexes were monitored to determine the depth of anesthesia. The experimental animal was placed on a heating pad to maintain core body temperature during the procedures. The head of the animal was fixed in an adaptor for the stereotaxic frame by ear and nose bars. Eye ointment was applied to both eyes to prevent ocular dehydration during anesthesia. Hair removal lotion was applied to the top of the head. After hair removal, the surface of the skin was disinfected with 70% ethanol. Then, the skin was removed from the top of the skull. Lidocaine solution (2%; Sigma-Aldrich, MO, USA) was dripped onto the periosteum. The periosteum was removed from the exposed area of the skull with a blade, and the area was scraped gently to establish a clean surface. To dry the surface of the skull, it was wiped with a cotton wool stick. After an area 3–4 mm in diameter had been chosen over the sensorimotor cortex, the skull was gently thinned using a pneumatic dental drill (Foredom, Blackstone Industries, Bethel, CT, USA). During this procedure, the surface was cooled by topical application of cold, sterile PBS. Debris was blown off with compressed air. When the bone was thin enough (indicated by its slight movement when it was gently pushed on), craniotomy was performed under a drop of sterile PBS. The surface of the dura mater was carefully wiped down and any accidental bleeding—caused by the craniotomy—was stopped with a Hemosponge (Goodwill Lifesciences, India) gelatin sponge immersed in sterile PBS. The cranial window was dried very carefully to remove excess fluid from the area. A glass coverslip (diameter: 5 mm, Thomas Scientific, Swedesboro, NJ, USA), which was previously soaked in 70% ethanol, was rinsed in PBS and applied to the surface of the dura mater to completely cover the cranial window. The coverslip was fixed to the skull with liquid adhesive and after the superglue had bonded, the cranial window was secured with Jet Set-4 dental acrylic resin (Lang Dental, Wheeling, IL, USA). The resin rim created a small pool around the cranial window. At the end of the surgery, the animals were treated with buprenorphine (1 mg/kg body weight, i.p.; Zoopharm, WY, USA). Enrofloxacin (5 mg/kg body weight, s.c.; Baytril, Bayer, Germany) was administered as a prophylactic antibiotic. The animals were closely monitored until the anesthesia wore off and they regained consciousness. Intravital imaging studies were conducted at least 2 to 3 weeks after surgery.

Intravital two-photon microscopy

Mice were anesthetized with 1.5–2.5% isoflurane (flow rate: 1 to 2 L/min) and placed on a heating pad. The head of the anesthetized animal was fixed in a stereotaxic frame. The blood plasma

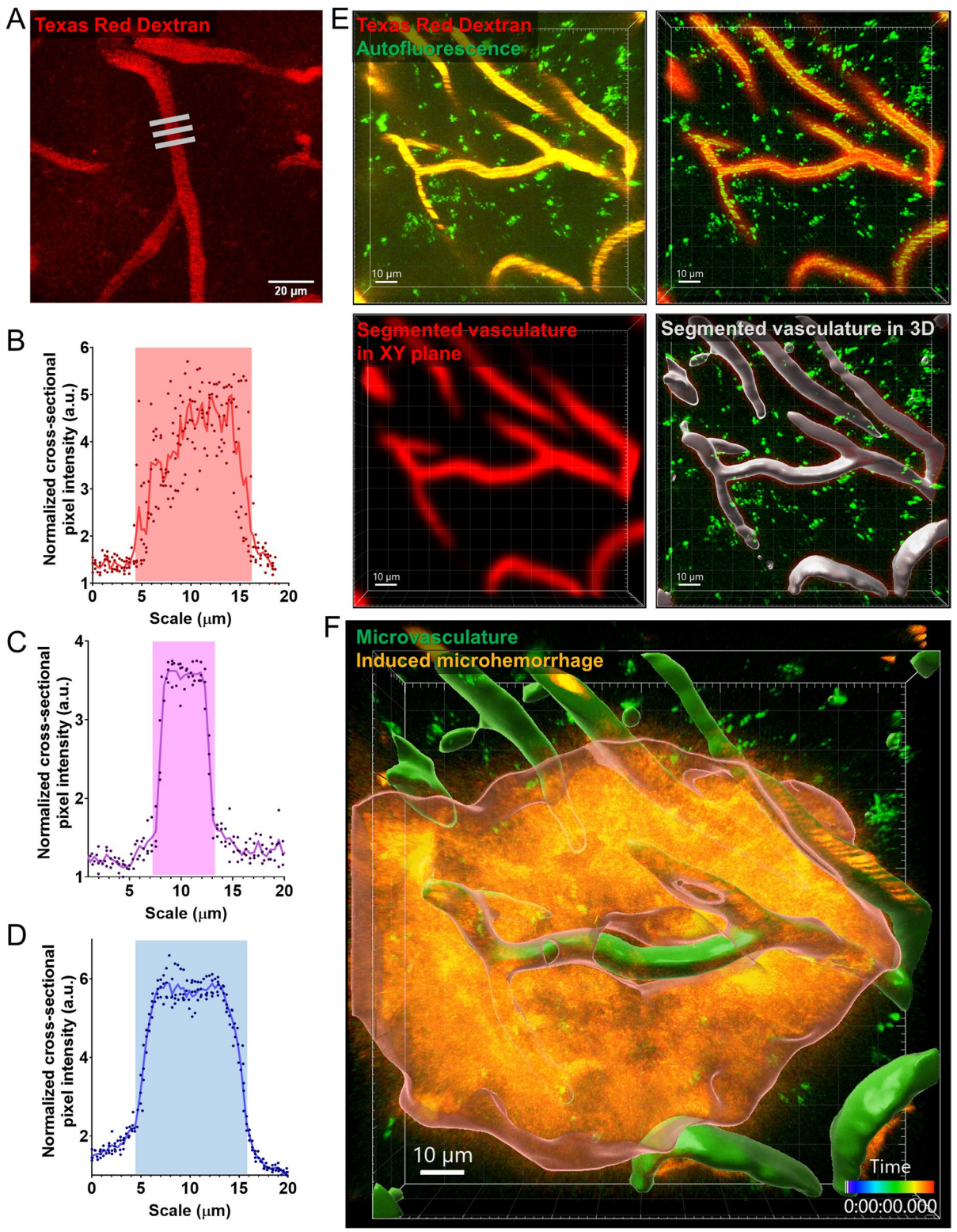
A
Texas Red Dextran
20 μm
B
Normalized cross-sectional pixel intensity (a.u.)
Scale (μm)
C
Normalized cross-sectional pixel intensity (a.u.)
Scale (μm)
D
Normalized cross-sectional pixel intensity (a.u.)
Scale (μm)
E
Texas Red Dextran
Autofluorescence
10 μm
10 μm
Segmented vasculature in XY plane
10 μm
Segmented vasculature in 3D
10 μm
F
Microvasculature
Induced microhemorrhage
10 μm
Time
0:00:00.000

◂**Fig. 2** Advanced in silico analysis of cerebral microvasculature and laser ablation-induced cerebral microhemorrhages (CMHs). **A** Representative image of vascular diameter measurement. Gray bars highlight areas where diameter measurements were. Scale bar: 20 µm. **B–D** Representative dot plots showing microvascular diameter measurements for arterioles, capillaries, and venules, respectively. The diameter was determined based on the cross-sectional intensity profile. **E** Stations of the in silico image analysis of microvasculature before ablation, depicting the analysis methods utilized in determining 3D vascular volume and morphology. **F** 3D segmentation of induced CMH separated from microvasculature and surrounding parenchyma. The z- and time-stacks were analyzed with IMARIS 3D segmentation method after excluding vasculature and background intensities. Scale 10 µm

was labeled with different fluorescent dextran-conjugated dyes (FITC-dextran 40 kDa, Texas Red-dextran 70 kDa and Cascade Blue-dextran 10 kDa, ThermoFisher Scientific, MA, USA; or SR101, Sigma Aldrich, MO, USA) all at a concentration of 8 mg/kg body weight, diluted in sterile saline and injected retro-orbitally before imaging. Imaging was performed with a FluoView 1000 MPE (Olympus, Tokyo, Japan) two-photon microscope coupled with a MaiTai HP DeepSee-OL 690–1040 nm (Spectra-Physics, San Jose, CA, USA) laser and equipped with a XLPLN25XWMP 25 × water immersion objective (1.05 numeric aperture; Olympus, Tokyo, Japan) with excitation at 800 nm. For some of the experiments, a NIKON A1R MP + Multiphoton Confocal Microscope System with a tunable Ti:Sapphire laser was used with a Dual line 1300 nm laser (Nikon Instruments Inc., NY, USA).

Induction of CMHs by high-energy laser light-induced photodisruption of arterioles, capillaries, and venules

We employed a laser ablation method to rupture targeted cerebral arterioles, venules, and capillaries. We identified the feeding arteries on the brain surface and traced them deeper into the brain parenchyma, identifying different parts of the branching vascular network that supplies the capillary beds (Fig. 1A, B). By analyzing the direction of blood flow, we distinguished arterioles from venules, using previously published methods [54]. Capillaries located between ~ 80 and 150 µm deep within the brain cortex were identified based on their diameter and the direction of blood flow relative to that in feeding arterioles. By injecting high-molecular-weight dextran dyes retro-orbitally, we visualized the blood flow direction based on the exclusion of red blood cells (RBCs) that appear as dark shadows (Fig. 1C–E). CMHs were induced using published protocols [55] and were recorded as follows. The number of ablation procedures required to rupture a vessel was largely dependent on the imaging depth and the clarity of the cranial window. Although we were able to image brain microvasculature as deep as ~ 600 µm within the cortex, to induce CMHs, we targeted vessels between 80 and 150 µm deep into the brain cortex (Fig. 1B, F). After an initial Z-stack of the target area had been captured, the edge of the targeted vessel was irradiated with a short burst of femtosecond laser pulses (pulse width of less than 100 fs) for 20 s at a laser power of 20%. Development of the CMHs was imaged with fast resonant scanner in either ZT-stack or high-resolution T-stack. If a CMH was not evident after the first try, the process was repeated up to three times until a CMH was successfully induced. If a CMH was not induced during the three trials, a different vessel at least 50 µm away was selected for ablation to avoid thermal damage to the neighboring brain tissue. Animals were longitudinally imaged to track the bleed size and healing rate.

Image reconstruction, image analysis, and quantification

Image analysis was performed with FIJI, ImageJ2 1.53f51 open version (Fig. 2A–D) and the commercially available version of the IMARIS 9.1 imaging software (Oxford Instruments, NY, USA) (Fig. 2E–F) to measure and reconstruct 3D Z-, and time (T)-stacks, determine CMH area and volume, measure vascular diameter and volume, and evaluate their time-dependent changes in these parameters. We also assessed fluorescent speckle displacement (to estimate CMH volume) and the pressure-induced

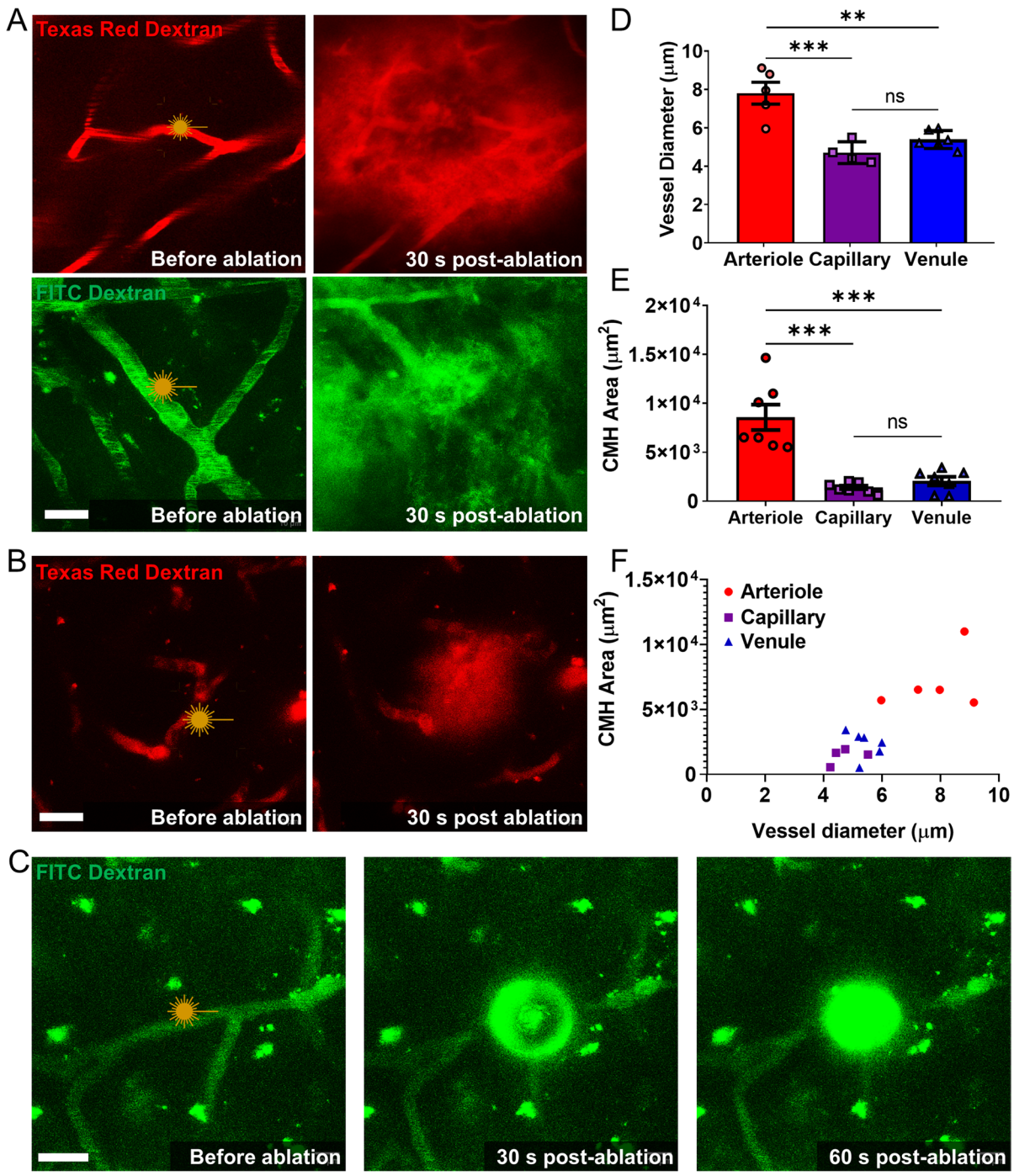
A
Texas Red Dextran
Before ablation
30 s post-ablation
FITC Dextran
Before ablation
30 s post-ablation
B
Texas Red Dextran
Before ablation
30 s post ablation
C
FITC Dextran
Before ablation
30 s post-ablation
60 s post-ablation
D
Vessel Diameter (μm)
Arteriole Capillary Venule
**
***
ns
E
CMH Area (μm²)
Arteriole Capillary Venule
***
***
ns
F
CMH Area (μm²)
Arteriole
Capillary
Venule
Vessel diameter (μm)

◂**Fig. 3** Vascular heterogeneity determines the size of cerebral microhemorrhages (CMHs). **A** Representative images of arteriolar CMHs, showing the distinct round and widespread morphology. Different dextran tracers were used, and all arteriole bleeds displayed this morphology. Scale: 20 µm. **B** A representative image of a venular CMH is displayed, demonstrating the diffuse morphology of venular bleeds, with the extravasated blood mostly remaining in the perivascular space. Scale: 20 µm. **C** A capillary bleed is shown, depicting a small round pressure wave observed from capillaries, with no tissue displacement or tracer spreading along the vessel. Scale: 20 µm. **C** Representative images showing induction of a small, round capillary CMH. No tissue displacement or tracer spreading along the vessel was evident. Scale bar: 20 µm. **D** The diameter differences in ablated cerebral microvessels are shown. The targeted arterioles were significantly larger than the venules and capillaries that were targeted. **E** The induced CMHs area distribution versus vessel of origin is depicted, showing significantly larger bleeds in the case of arteriolar CMHs. **F** The CMH area is plotted as a function of vessel diameter, showing that bleeds cluster by the vessel of origin. The presented data are the mean ± SEM; *$p < 0.05$, **$p < 0.01$, ***$p < 0.001$

reduction of intravascular staining ("halo" region) around the CMHs. Image analysis started with the elimination of the background. Next, the object was determined by dimension reduction in 2D (e.g., maximal intensity projection of Z- and T-stacks) or 3D segmentation with the "Surfaces" adaptive segmentation algorithm of the IMARIS imaging software. Segmentation of the different channels was combined, and empty channels were also used as background reference. As a last step, vascular diameter, CMH expansion, and speckle displacement were measured on the processed, reconstructed images. Results were cross-validated in FIJI and IMARIS.

Statistical analysis

Data are presented as mean ± standard error of the mean (SEM) unless stated otherwise. Statistical analysis was performed with GraphPad Prism 8.0.1 software (Dormatics, San Diego, CA, USA). Student two-sample *t*-test, pairwise *t*-test, or one-way ANOVA with Fisher LSD post hoc test was performed, as appropriate to compare experimental results. Differences were considered significant at $p < 0.05$. Each datapoint was derived from at least three independent measurements ($n \geq 3$, exact "*n*" numbers are indicated in the figure legends).

Results

Laser ablation-induced CMHs in the mouse brain

To disrupt microvessels in the cerebral cortex while minimizing the impact on the surrounding parenchyma, we used a method of in vivo photodisruption targeting deep-lying vessels in mice with chronic cranial windows [52]. By utilizing high-energy, ultrashort pulses of laser light (from our two-photon microscope) at the objective's focus, nonlinear interactions can occur within a femtoliter-sized volume, causing ionization and resulting in disruption of the cells constituting the microvascular wall [52]. Arterioles, capillaries, and venules to be targeted for CMH induction were identified based on their location, direction of blood flow (Fig. 1), and diameter (Fig. 2). Representative images in Fig. 1F show the development of CMHs upon high-energy laser light-induced photodisruption of a targeted arteriole. Representative images in Fig. 2E–F depicts the 3D segmentation of an induced CMH and its spatial relationship to the microvasculature.

Relationship between size of CMHs and type and diameter of vessel of origin

To establish the relationship between type/size of the vessel of origin and size of the CMHs, high-energy laser light-induced photodisruption of arterioles, capillaries, and venules was performed in the somatosensory cortex of young mice (Fig. 3A–C). Figure 3D shows the diameter of each vessel type (measured prior to CMH induction). Figure 3E shows CMH sizes for each vessel type (measured 30 s after CMH induction). We found that CMHs originating from arterioles were significantly larger than CMHs originating from both capillaries and venules. The size of CMHs correlates with the diameter of the vessel of origin

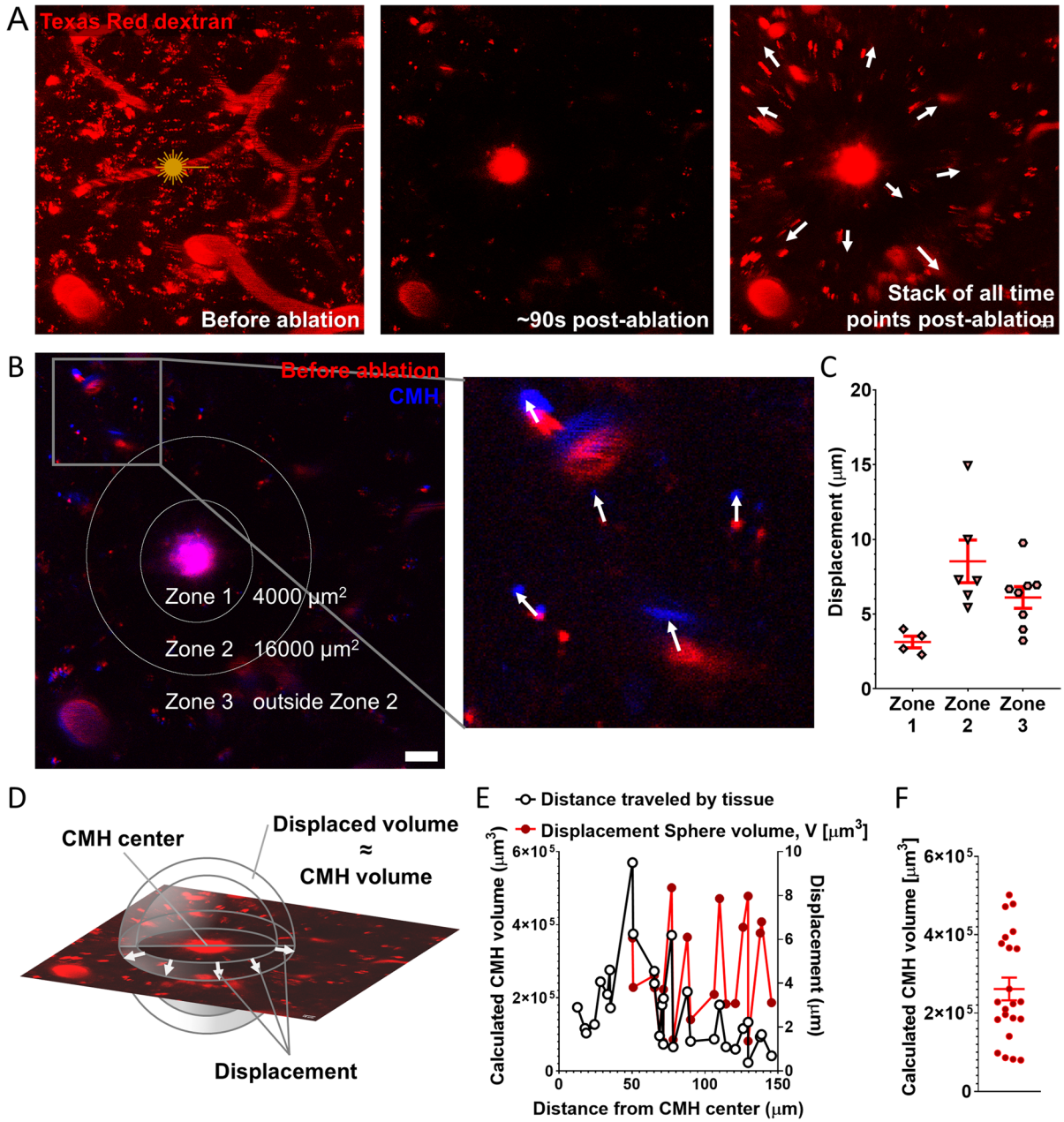

Fig. 4 Arteriolar cerebral microhemorrhages (CMHs) cause brain tissue displacement affecting surrounding cells and vasculature. **A** Representative timelapse images of an arteriolar CMH over a period of 90 s, showing significant pressure-induced tissue displacement. Arrows indicate the direction of movement of objects traced in the timelapse images. Scale: 20 µm. **B** Image of the area of photoablation before induction of CMH in red, and after induction of CMH in blue, with an overlap showing tissue displacement. Arrows indicate the direction of displacement based on the moving objects. Scale: 20 µm. **C** Comparison of three zones around the laser ablation-induced CMH based on the magnitude of tissue displacement. Data are mean ± SEM. **D** Mathematical background of the estimation of the CMH volume from the displacement of objects. The displacement length determines a spherical shell, whose volume reflects the volume of the CMH. **E** Volume of the CMH, calculated based on the volume of the spherical shells defined by the displacement of individual objects traced in the timelapse images, plotted as a function of their distance from the site of ablation. Zones 2 and 3 were used to calculate the volume of the spherical shells. The standard deviation results from the geometric divergence of the maximal projection from 3 to 2D. **F** Estimation of CMH volume based on the average of the calculated volumes of the spherical shells. The estimated volume of this representative arteriolar CMH is 2.6×10^5 µm^3

(Fig. 3F). We found that arteriolar CMHs were the largest, with CMH cross-sectional areas in maximum intensity projections ranging from 5000 μm^2 (~36 μm radius) to 10,000 μm^2 (~57 μm radius) (Fig. 3A, E). Arteriolar CMHs typically exhibited a spherical morphology. Capillary CMHs were the smallest with bleed areas ranging from 500 to 2000 μm^2 on maximal intensity projections (Fig. 3C, E, F). Capillary bleeds were also typically spherical. In contrast, venular CMHs were more diffuse and irregular in shape, often spreading in the perivascular space, with CMH cross-sectional areas in maximum intensity projections ranging from 600 to 3000 μm^2 (Fig. 3B, E).

CMH-induced compression of neuronal tissue

Development of larger CMHs originating from arterioles was associated with significant displacement of the neighboring brain tissue (Fig. 4,) which was not observed with bleeds originating from capillaries or venules. Images were captured prior to and ~90 s after induction of CMH, and tissue displacement was measured by tracking the movement of fluorescently labeled vessels and other autofluorescent puncta in the neighboring brain tissue (Fig. 4B, C; in 4B, baseline fluorescence is shown in red, while fluorescence at 90 s post-CMH is shown in blue). Tissue displacement was highest in zone 2, an area ranging from 35 to 70 μm from the center of the bleed (Fig. 4B, C). The volume of each CMH (V_{CMH}) was calculated as: $V_{CMH}=4/3\times(\pi\times {r_2}^3-\pi\times {r_1}^3)$, where r_1 is the distance of a fluorescent speckle from the center of the CMH before ablation, and r_2 is the distance of the same fluorescent speckle from the center of the CMH post-ablation (Fig. 4D–F).

We noticed that increased pressure within the brain tissue due to the development of arteriolar CMHs resulted in a decline in capillary staining in the brain area surrounding the CMH (Fig. 5A, observe dark ring around induced CMH), likely due to compression and constriction of these microvessels. To estimate the area of brain tissue which is potentially at risk of ischemia due to the impairment of microcirculatory blood flow following a CMH, large high-resolution Z-stack images were captured (Fig. 5A–C). In these images, the area with decreased capillary staining was identified (Fig. 5D, orange circle). In Fig. 5F, the radial fluorescent intensity profile is shown, reflecting a dramatic drop in fluorescence from the center of the bleed to the immediately adjacent area before beginning to recover. The area at highest risk corresponds to the zone with the largest pressure-induced tissue compression (Fig. 5E) and the lowest capillary staining intensity (Fig. 5F), extending from ~35 to 70 μm from the center of the bleed; however, the affected area continues up to ~100 μm in each direction before fluorescence (reflecting blood flow) recovers (Fig. 5F).

CMHs induce constriction of capillaries and precapillary arterioles

The effect of CMHs on the diameter of neighboring microvessels was analyzed in time series images. Upon induction of arteriolar CMHs and most capillary CMHs, prompt constriction of neighboring capillaries and precapillary arterioles was evident. Of note, this phenomenon was not observed in association with 25% of the smaller capillary CMHs. Figure 6A and B show constriction of a precapillary arteriole in the brain of a MYH11^{tdTomato} mouse in response to the induction of an arteriolar CMH. Note the constriction of the MYH11^{tdTomato} positive red fluorescent mural cells. After image segmentation (Fig. 6B), the dynamics of the progression of CMH and simultaneous constriction of the precapillary arteriole was plotted (Fig. 6C). Summary data (Fig. 6D) show that CMHs elicited significant constriction in neighboring microvessels. We also compared changes in the diameter of vessels upstream and downstream from the CMHs. Representative images in Fig. 6E and the line intensity scans in Fig. 6F show that induction of CMHs elicits similar constriction both in vessels proximal and distal to the CMHs (summary data are shown in Fig. 6G).

Demonstration of reactive astrogliosis and resolution of CMHs

To visualize reactive astrogliosis and resolution of CMHs, sulforhodamine 101 (SR101) was retro-orbitally injected in the experimental animals before the induction of CMHs. Upon laser light ablation,

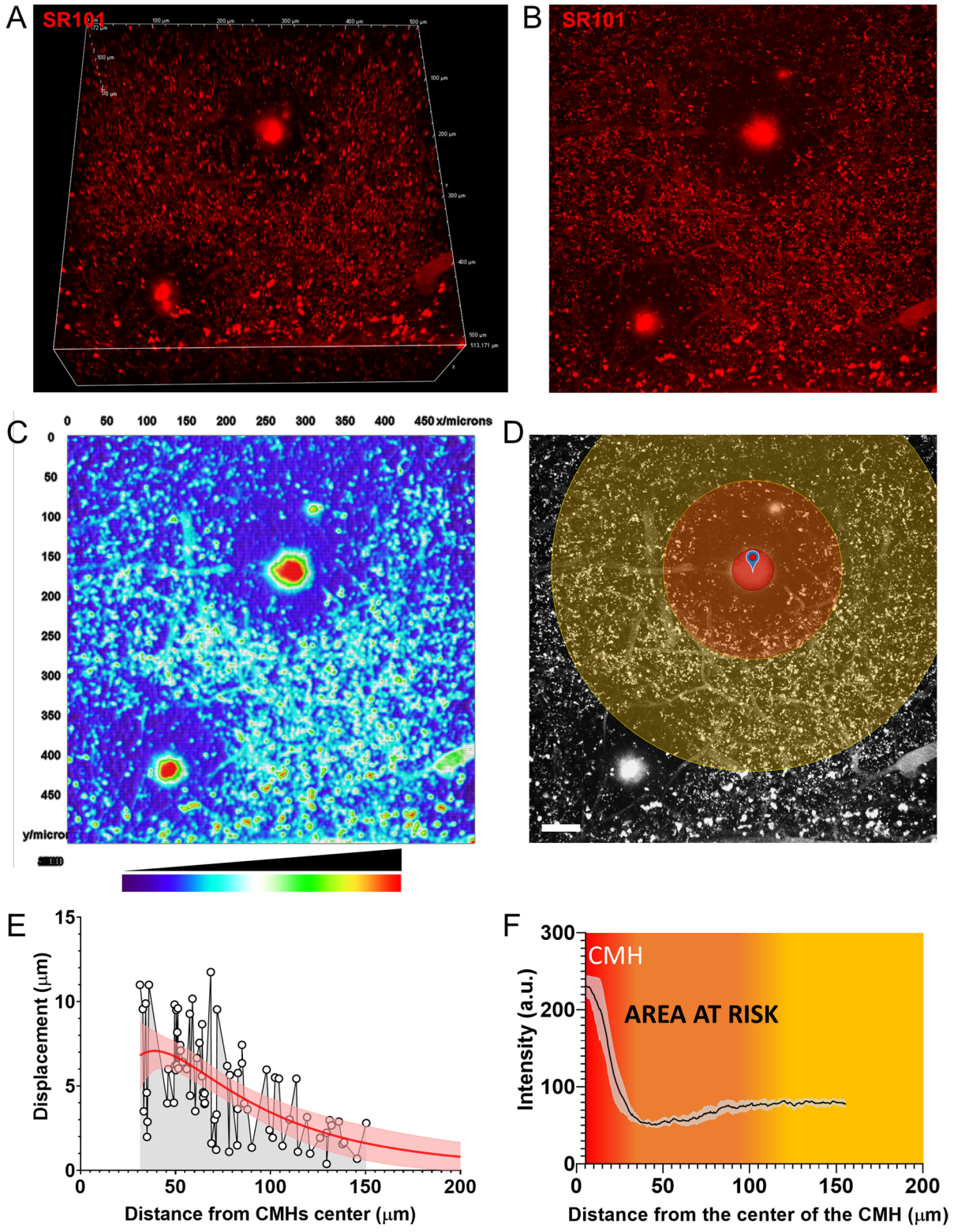
A
SR101
B
SR101
C
0 50 100 150 200 250 300 350 400 450 x/microns
0
50
100
150
200
250
300
350
400
450
y/microns
D
E
Displacement (μm)
0
5
10
15
0 50 100 150 200
Distance from CMHs center (μm)
F
Intensity (a.u.)
0
100
200
300
CMH
AREA AT RISK
0 50 100 150 200
Distance from the center of the CMH (μm)

◂**Fig. 5** Estimation of area at risk in the brain after induction of cerebral microhemorrhages (CMHs). **A** A 3D view, **B** a maximal intensity projection, and **C** a false color intensity map of two arteriolar CMHs with pressure-induced halos caused by reduced intravascular staining (due to compression of microvessels), which reveal the extent of the area affected by the CMHs. **D** The pressure-induced compression zones after induction of the arteriolar CMHs (see **F**). The scale of the image is 50 µm. **E** The length of object displacement as a function of distance from the center of the CMH. It is estimated that the most significant compression of the brain tissue surrounding the CMH occurs up to a distance of ~ 80 µm from the center of the CMH. **F** The radial intensity profile obtained from measurements on the maximal intensity projections (**D**) of the brain area surrounding the CMH ($n = 4$). The zone representing an area of the brain with compressed microvessels ("area at risk"; color-coded orange) extends to ~ 80 µm around the arteriolar CMH

extravasation of SR101 could be imaged to monitor the development of CMH (Figs. 7A and 8A). Extravasated SR101 was subsequently taken up by astrocytes [56–59]. Over the course of several days, reactive astrogliosis at the site of the CMH could be visualized by longitudinal imaging (Figs. 7B and 8B). Reactive astrogliosis in the adult mouse brain reached its peak on day 5 before gradually diminishing over the 30-day observation period, aligning with the resolution of the CMH (Fig. 7B and C). Conversely, in the aged cerebral cortex, a decline in astrogliosis was not observed, as illustrated in Fig. 8B and C. This disparity corresponds to impaired CMH clearance, sustained astrogliosis, and potential inflammation at the initial CMH location within the aged cerebral cortex.

Discussion

In this study, we utilized multiphoton imaging and laser ablation techniques to investigate the variations in CMH morphology arising from different vascular locations. Our findings demonstrate striking similarities between the bleed morphologies observed in hypertension-induced CMHs in models of aging from previous preclinical studies [42–44, 51, 60] and those originating from different vessels targeted via multiphoton laser ablation. Our results suggest that arteriolar bleeds, which are larger (> 100 µm in diameter) and more widely dispersed, are distinguished from venular bleeds, which are smaller and exhibit a distinct diffuse morphology. Moreover, we can infer that capillary bleeds are circular and smaller (< 10 µm in diameter) in size. Our study confirms that microbleeds can occur at any point in the vascular tree, with each vessel type producing microbleeds with a unique morphology.

Understanding the vessel-of-origin of a CMH can provide insight into pathophysiological mechanisms (e.g., providing evidence for the role of penetration of arterial pressure to the thin-walled distal part of the microcirculation in aging or increases in venous pressure due to venous congestion). Our study provides much-needed data for the development of a reliable method for identifying microbleed sources based on morphology and will help answer the question of which branch of the vascular tree is most susceptible to CMHs in aging and pathological conditions associated with accelerated microvascular aging. Our results demonstrate that vessel type determines CMH shape and morphology, and vessel size alone does not dictate the size or shape of a bleed [61, 62]. For example, venules produced smaller bleeds than comparable arterioles and venular bleeds often diffused into the perivascular space. The likely explanation for these differences is that intravascular pressure drops drastically along the microvascular network, from small arteries to veins. The difference in CMH morphology likely reflects differences in intravascular pressure, not just vessel size. Future studies should investigate the prevalence of different CMH types (arteriolar vs venular vs capillary) in the aged brain and their specific impact on the neurovascular microenvironment. In particular, studies on genetic animal models of aging [42, 43] will be able to identify specific pathways contributing to increased vascular fragility at different levels of the cerebral microcirculation. MRI techniques that are commonly used to detect CMHs (SWI, GRE imaging) have a high spatial resolution that can detect lesions as small as a few millimeters in diameter. As the resolution of neuroimaging

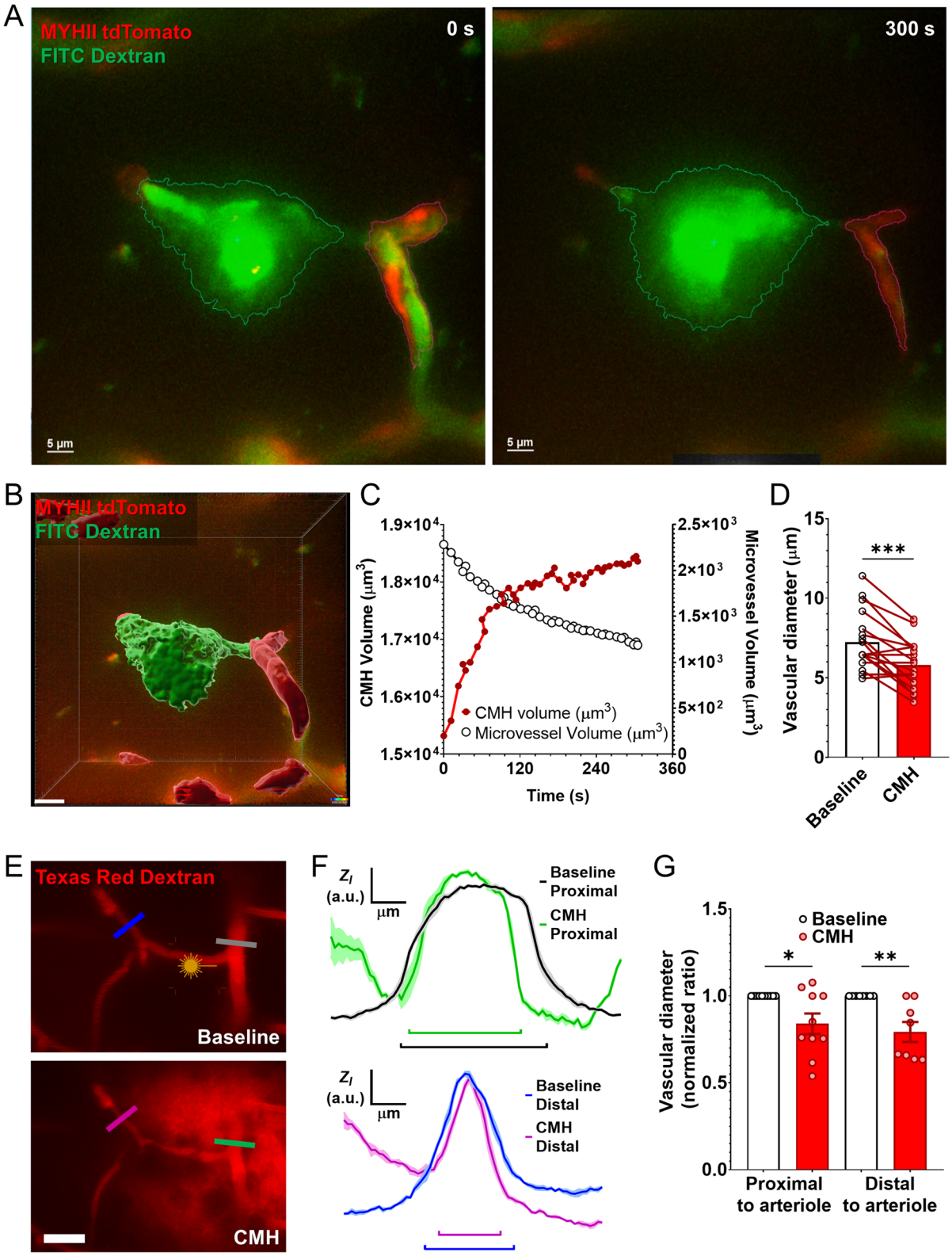
A
MYHII tdTomato
FITC Dextran
0 s
300 s
5 µm
5 µm
B
MYHII tdTomato
FITC Dextran
C
CMH Volume (µm³)
Microvessel Volume (µm³)
1.9×10⁴
1.8×10⁴
1.7×10⁴
1.6×10⁴
1.5×10⁴
2.5×10³
2×10³
1.5×10³
1×10³
5×10²
0
0
120
240
360
Time (s)
CMH volume (µm³)
Microvessel Volume (µm³)
D
Vascular diameter (µm)
15
10
5
0
***
Baseline
CMH
E
Texas Red Dextran
Baseline
CMH
F
Zl (a.u.)
µm
Baseline Proximal
CMH Proximal
Baseline Distal
CMH Distal
G
Vascular diameter (normalized ratio)
1.5
1.0
0.5
0.0
Baseline
CMH
*
**
Proximal to arteriole
Distal to arteriole

◂**Fig. 6** Development of cerebral microhemorrhages (CMHs) is associated with prompt constriction of neighboring microvessels. **A** Representative image of a microvessel in the brain of a MYH11^{tdTomato} mouse after laser ablation and 300 s later. The tdTomato labels the vascular mural cells (potential ensheathing pericytes), and the vascular lumen was filled with FITC-dextran tracer to track the development of the CMH. Note the increased area of the bleed and reduced area of the tdTomato labeling. **B** The 3D segmentation and **C** the analysis of the tracking of the induced CMH over time. The vascular lumen has continuously decreased and tended to reach a minimum as the size of the CMH reached a plateau phase. The scale of the image is 10 µm. **D** The vascular diameter changes after induction of arteriolar CMHs. Baseline and post-ablation diameters have been measured and plotted for pairwise and pooled comparison ($n = 18$ total measurements). **E** Representative images, **F** the analysis, and **G** the quantification of vascular diameter changes of vascular segments proximal and distal to the induced CMHs. The color-coded lines show the measurement area of the targeted vessels. Note the significantly reduced diameter in both proximal and distal vascular branches. Data are mean ± SEM; $*p < 0.05$, $**p < 0.01$, $***p < 0.001$ ($n = 10$ proximal, $n = 8$ distal)

techniques improves, it becomes increasingly feasible to conduct neuroimaging-pathological correlation studies, which can facilitate the translation of our findings into clinical research applications. Yet, there are still many challenges. Accurately estimating the size of CMHs using MRI can be challenging due to factors such as the shape of the lesion and the susceptibility effects of surrounding tissues. The "blooming" effect seen on SWI and GRE images can make the size of the lesion appear larger than it actually is, which can lead to overestimation of the lesion size. In addition, the spatial resolution of MRI can also affect the accuracy of size estimation, as smaller lesions may be more difficult to distinguish from noise or artifacts.

Our study also provides additional evidence in support of the concept that arteriolar CMHs may have a larger impact than just the disruption at the point of arteriolar rupture. Tissue displacement observed in association with arteriolar CMHs suggests that they can affect an area with a radius of ~ 50 µm to ~ 100 µm (Figs. 4 and 5). The tissue displacement around the developing arteriolar CMHs in the enclosed space of the skull compresses neighboring microvessels, which impedes blood flow likely impairing oxygen and nutrient delivery to the surrounding neuronal tissue. This adverse effect is also exacerbated by the induction of significant capillary constriction in response to microbleeds (Fig. 6). This phenomenon was predominantly seen in capillary CMHs. Capillary constriction may be the result of the constriction of capillary pericytes in response to vasoconstrictor substances released from aggregating thrombocytes (e.g., prostaglandin H_2, thromboxane A_2, serotonin, leukotriens [63]) in the leaked blood. Although pericyte function was not specifically investigated in our study, other studies have highlighted the important role of pericytes in vasoconstriction in various organs during pathological scenarios such as ischemia–reperfusion, as well as in blood flow regulation through bi-directional control of CNS capillaries [64–69]. While the complete duration of CMH-related capillary constriction is unknown, this observation adds to the growing evidence that CMHs are associated with changes in regional blood flow regulation that affects a brain area way beyond the territory impacted by the bleeding per se. This "area at risk" (due to compression-mediated decline in capillary flow and induced capillary constriction) may contribute to the development of temporal, perhaps often subclinical, neuronal symptoms (e.g., changes in motor function, TIA-like symptoms) which would potentially resolve when regional blood flow is re-established. It is possible that this "area at risk" could be vulnerable to permanent damage in the presence of other risk factors compromising timely recovery of regional blood flow (e.g., in Alzheimer's disease). With advancing age, the ability of the microvascular network to adapt and redirect blood flow in response to regional blockages may diminish. As a result, even minor CMHs arising from the capillaries could trigger a cascade of disrupted blood flow and further blockages over time. In addition, microbleeds can adversely affect essential homeostatic processes like neurovascular coupling. CMHs and the related inflammatory reaction may disrupt the regulation of regional cerebral blood flow, resulting in a sustained imbalance between the supply and demand of oxygen and nutrients [70, 71].

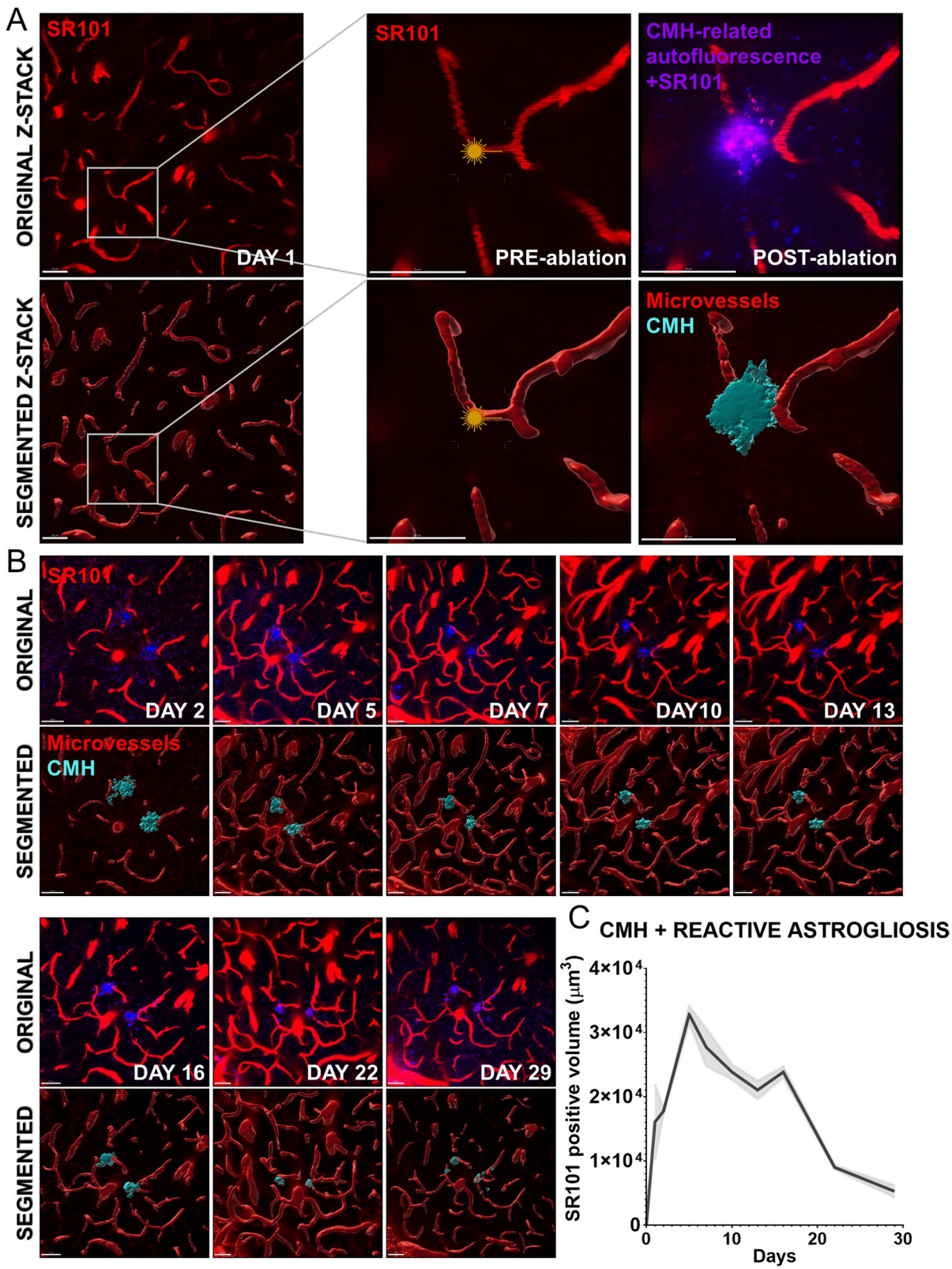
A
ORIGINAL Z-STACK
SEGMENTED Z-STACK
SR101
DAY 1
SR101
PRE-ablation
CMH-related autofluorescence +SR101
POST-ablation
Microvessels
CMH
B
ORIGINAL
SEGMENTED
SR101
DAY 2
DAY 5
DAY 7
DAY10
DAY 13
Microvessels
CMH
DAY 16
DAY 22
DAY 29
C
CMH + REACTIVE ASTROGLIOSIS
SR101 positive volume (μm3)
4×10⁴
3×10⁴
2×10⁴
1×10⁴
0
0
10
20
30
Days

◂**Fig. 7** Longitudinal tracking of laser ablation-induced cerebral microhemorrhages (CMHs) and surrounding reactive astrogliosis in adult mice. **A** Representative figures of original and 3D segmentation of brain microvessels before and right after the induction of CMH in adult mice. Note the extravasation of the fluorescent tracer dye SR101 upon disruption of the microvascular wall. SR101 is a Texas red analog dye that specifically labels astrocytes, making it a useful tool for studying the reactive astrogliosis associated with CMHs in longitudinal tracking experiments. Scale: 50 µm. **B** Representative images of the longitudinal tracking of the induced CMHs for 1 month. **C** Quantification of the 3D SR101 positive volume (consisting of the CMHs and areas of reactive astrogliosis) associated with the tracked CMHs as a function of time. Note the gradual decline in SR101 positive volume after ~ 2 weeks post-ablation corresponding to the resolution of the CMHs

In response to CMHs, astrocytes in the surrounding tissue become activated, proliferate and undergo hypertrophy, a process known as reactive astrogliosis [72]. This leads to an increase in astrocyte number and their reorganization around the site of injury. Reactive astrocytes also secrete various cytokines and growth factors that promote inflammation, angiogenesis, and tissue remodeling. Importantly, our study found that astrogliosis after CMHs persisted for 30 days suggesting the potential long-term impact of microbleeds and the subsequent inflammatory response on the neurovascular environment. While astrogliosis is an important component of the brain's response to injury, chronic and excessive astrogliosis can have detrimental effects on brain function, including neuronal death and impaired synaptic plasticity. Our findings demonstrate a notable distinction between aged and adult mice regarding the resolution of cerebral CMHs within the cerebral cortex. In aged mice, there is a significant delay in the resolution of CMHs, potentially indicating impairment in the clearance process. This delayed resolution not only sustains, but also exacerbates local inflammation and astrogliosis within the aged brain subsequent to CMH occurrence.

While our study examined the role of reactive astrogliosis and inflammation in the pathophysiology of CMHs within the cerebral cortex, it is crucial to acknowledge that the involvement of other cell types, particularly oligodendrocytes, in CMH-related neurovascular pathologies requires further investigation. Previous research has shed light on the potential significance of oligodendrocytes in white matter injury and its connection to impaired vasodilator function of white matter arterioles [73]. Additionally, studies have highlighted the impact of ineffective oligodendrocyte precursor cell maturation on age-related defective remyelination processes [74–78]. While not the primary focus of our current investigation, these findings underscore the intricate cellular mechanisms at play and suggest that future studies should explore the specific contributions of oligodendrocytes in CMH-related CNS pathologies.

One limitation of our study is the difficulty in inducing and recording CMHs in deeper brain regions using the chronic cranial window model. However, with the rapid advancements in microscopy techniques, future investigations can explore the possibility of inducing CMHs in deeper brain regions, including the white matter, in order to examine whether vessel-dependent differences in microbleed morphology hold true across all brain regions. Numerous studies have highlighted the significance of white matter abnormalities, such as hyperintensities and diffusion changes associated with aging, as key drivers of cerebrovascular disease that ultimately contribute to cognitive decline [70, 79–82]. While our study did not specifically delve into neuronal depression or the impact of astrocytes on remote vasoconstrictions, it is important to acknowledge previous research by others that has established the role of hypoperfusion and hypoxia in neuronal depression, particularly in the context of aging [83–85]. Future experiments should aim to investigate the role of CMHs in both white matter damage and neuronal dysfunction, shedding further light on these important aspects of CMH-related pathologies.

In conclusion, our findings provide compelling evidence for the potential utility of analyzing CMH size and morphology and provide basis for further preclinical investigations aimed at elucidating the underlying mechanisms of age-related microvascular fragility and optimizing treatment strategies for the prevention of CMHs in aging.

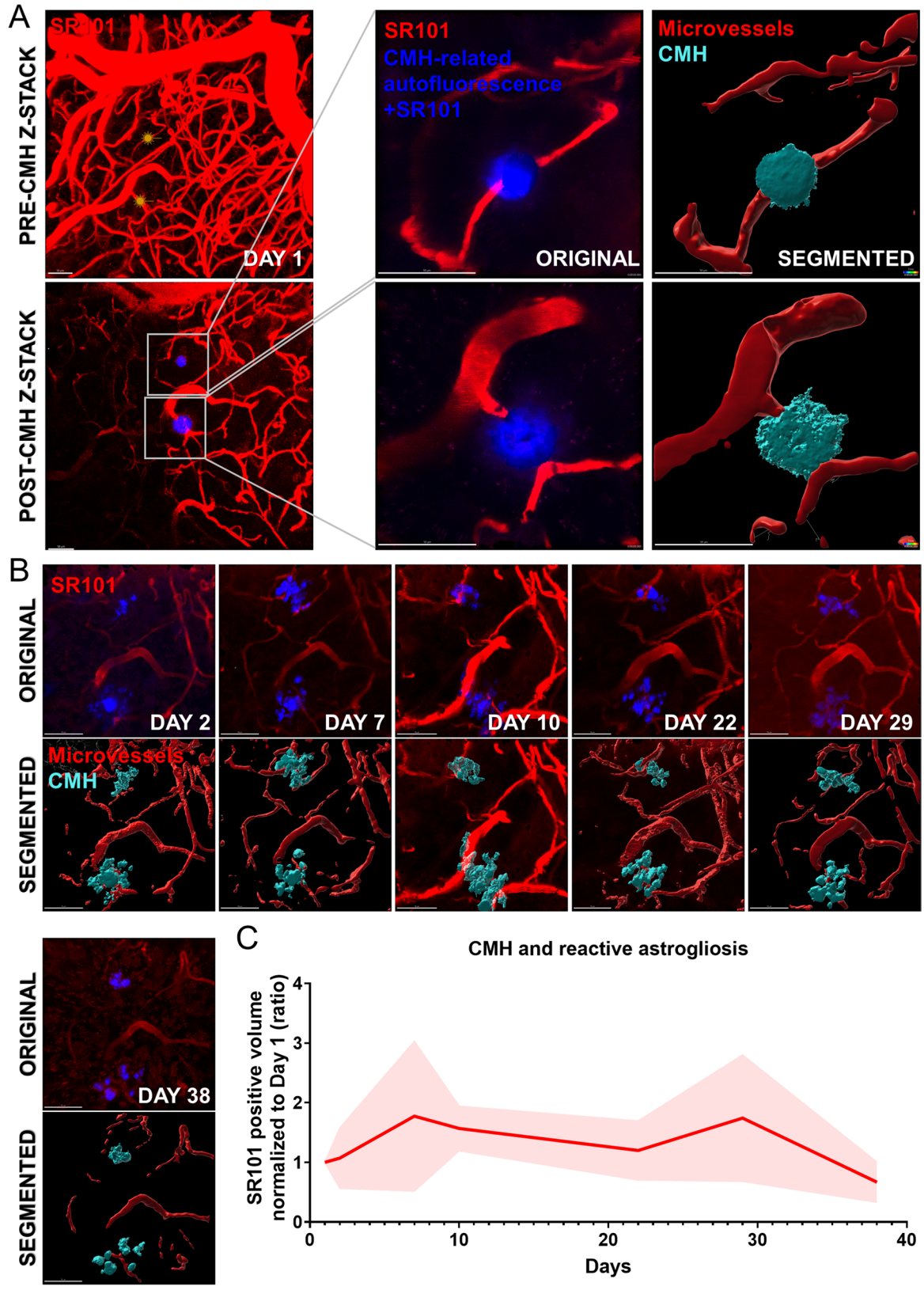
A
PRE-CMH Z-STACK
POST-CMH Z-STACK
SR101
DAY 1
SR101
CMH-related
autofluorescence
+SR101
ORIGINAL
Microvessels
CMH
SEGMENTED
B
ORIGINAL
SEGMENTED
SR101
DAY 2
DAY 7
DAY 10
DAY 22
DAY 29
Microvessels
CMH
ORIGINAL
SEGMENTED
DAY 38
C
CMH and reactive astrogliosis
SR101 positive volume
normalized to Day 1 (ratio)
0
1
2
3
4
0
10
20
30
40
Days

◂**Fig. 8** Longitudinal tracking of laser ablation-induced cerebral microhemorrhages (CMHs) and surrounding reactive astrogliosis in aged mice. **A** Representative figures of original and 3D segmentation of brain microvessels before and right after the induction of CMH in brain of an aged (24-month-old) mouse. Note the extravasation of the fluorescent. tracer dye SR101 upon disruption of the microvascular wall. Scale: 50 μm. **B** Representative images of the longitudinal tracking of the induced CMHs for 38 days in 24-month-old mouse. **C** Quantification of the 3D SR101 positive volume (consisting of the CMHs and areas of reactive astrogliosis) associated with the tracked CMHs as a function of time in brains of aged mice. It is noteworthy that the gradual decline in SR101-positive volume, which is observed in younger mice approximately 2 weeks post-ablation, is not evident in aged mice. This observation suggests that the resolution of CMHs is impaired in aged mice, leading to sustained astrogliosis. This sustained astrogliosis likely contributes to a heightened state of neuroinflammation within the aged brain

Funding This work was supported by grants from the American Heart Association (ANT: AHA834339), the Oklahoma Center for the Advancement of Science and Technology, the National Institute on Aging (RF1AG072295, R01AG055395, R01AG068295; R01AG070915, K01AG073614), the National Institute of Neurological Disorders and Stroke (R01NS100782), the National Cancer Institute (R01CA255840), the Oklahoma Shared Clinical and Translational Resources (U54GM104938) with an Institutional Development Award (IDeA) from NIGMS, the Presbyterian Health Foundation, the Reynolds Foundation, the Oklahoma Nathan Shock Center (P30AG050911), and the Cellular and Molecular GeroScience CoBRE (P20GM125528). PT was also supported by grants from the National Research, Development and Innovation Office (OTKA K-134555), the Hungarian Academy of Sciences Bolyai Research Scholarship, National Clinical Neuroscience Laboratory (RRF-2.3.1–21-2022–00011), and the Thematic Excellence Program 2021 Health Sub-programme of the Ministry for Innovation and Technology in Hungary, within the framework of the EGA-16 project of the University of Pecs. Support was also provided by Project no. TKP2021-NKTA-47, implemented with the support provided by the Ministry of Innovation and Technology of Hungary from the National Research, Development and Innovation Fund, financed under the TKP2021-NKTA funding scheme; by funding through the National Cardiovascular Laboratory Program (RRF-2.3.1–21-2022–00003) provided by the Ministry of Innovation and Technology of Hungary from the National Research, Development and Innovation Fund; Project no. 135784 implemented with the support provided from the National Research, Development and Innovation Fund of Hungary, financed under the K_20 funding scheme and the European University for Well-Being (EUniWell) program (grant agreement number: 101004093/ EUniWell/EAC-A02-2019 / EAC-A02-2019–1). The funding sources had no role in the study design; in the collection, analysis, and interpretation of data; in the writing of the report; and in the decision to submit the article for publication.

Declarations

Competing interests Dr. Anna Csiszar serves as Associate Editor for The Journal of Gerontology, Series A: Biological Sciences and Medical Sciences and GeroScience. Dr. Zoltan Ungvari serves as Editor-in-Chief for GeroScience and as Consulting Editor for The American Journal of Physiology-Heart and Circulatory Physiology. Dr. Stefano Tarantini, Dr. Shannon Conley and Dr. Andriy Yabluchanskiy serve as Associate Editors for GeroScience.

Disclaimer The content is solely the responsibility of the authors and does not necessarily represent the official views of the National Institutes of Health, the American Heart Association, or the Presbyterian Health Foundation.

References

1. Akoudad S, et al. Cerebral microbleeds and the risk of mortality in the general population. Eur J Epidemiol. 2013;28(10):815–21.
2. Akoudad S, et al. Cerebral microbleeds are associated with an increased risk of stroke: the Rotterdam study. Circulation. 2015;132(6):509–16.
3. Akoudad S, et al. Association of cerebral microbleeds with cognitive decline and dementia. JAMA Neurol. 2016;73(8):934–43.
4. Ayaz M, et al. Imaging cerebral microbleeds using susceptibility weighted imaging: one step toward detecting vascular dementia. J Magn Reson Imaging. 2010;31(1):142–8.
5. Benedictus MR, et al. Microbleeds, mortality, and stroke in Alzheimer disease: the MISTRAL study. JAMA Neurol. 2015;72(5):539–45.
6. Chai C, et al. Increased number and distribution of cerebral microbleeds is a risk factor for cognitive dysfunction in hemodialysis patients: a longitudinal study. Medicine (Baltimore). 2016;95(12):e2974.
7. Cordonnier C, et al. Prevalence and severity of microbleeds in a memory clinic setting. Neurology. 2006;66(9):1356–60.
8. De Reuck JL, et al. The significance of cortical cerebellar microbleeds and microinfarcts in neurodegenerative and cerebrovascular diseases. a post-mortem 7.0-tesla magnetic resonance study with neuropathological correlates. Cerebrovasc Dis. 2015;39(2):138–43.
9. Fisher M, et al. Cerebral microbleeds in the elderly: a pathological analysis. Stroke. 2010;41(12):2782–5.
10. Goos JD, et al. Incidence of cerebral microbleeds: a longitudinal study in a memory clinic population. Neurology. 2010;74(24):1954–60.

11. Gregg NM, et al. Incidental cerebral microbleeds and cerebral blood flow in elderly individuals. JAMA Neurol. 2015;72(9):1021–8.
12. Poels MM, et al. Incidence of cerebral microbleeds in the general population: the Rotterdam Scan study. Stroke. 2011;42(3):656–61.
13. Poels MM, et al. Cerebral microbleeds are associated with worse cognitive function: the Rotterdam Scan study. Neurology. 2012;78(5):326–33.
14. Valenti R, et al. Cerebral microbleeds in patients with mild cognitive impairment and small vessel disease: the Vascular Mild Cognitive Impairment (VMCI)-Tuscany study. J Neurol Sci. 2016;368:195–202.
15. Shams S, et al. Cerebral microbleeds: different prevalence, topography, and risk factors depending on dementia diagnosis-the Karolinska Imaging Dementia study. AJNR Am J Neuroradiol. 2015;36(4):661–6.
16. Wiegman AF, et al. Cerebral microbleeds in a multiethnic elderly community: demographic and clinical correlates. J Neurol Sci. 2014;345(1–2):125–30.
17. Romero JR, et al. Risk factors, stroke prevention treatments, and prevalence of cerebral microbleeds in the Framingham Heart study. Stroke. 2014;45(5):1492–4.
18. Jia Z, et al. Hypertension increases the risk of cerebral microbleed in the territory of posterior cerebral artery: a study of the association of microbleeds categorized on a basis of vascular territories and cardiovascular risk factors. J Stroke Cerebrovasc Dis. 2014;23(1):e5-11.
19. Gao Z, et al. Cerebral microbleeds are associated with deep white matter hyperintensities, but only in hypertensive patients. PLoS ONE. 2014;9(3):e91637.
20. Benedictus MR, et al. Specific risk factors for microbleeds and white matter hyperintensities in Alzheimer's disease. Neurobiol Aging. 2013;34(11):2488–94.
21. Van der Flier WM, Cordonnier C. Microbleeds in vascular dementia: clinical aspects. Exp Gerontol. 2012;47(11):853–7.
22. Werring DJ, Gregoire SM, Cipolotti L. Cerebral microbleeds and vascular cognitive impairment. J Neurol Sci. 2010;299(1–2):131–5.
23. Ungvari Z, et al. Cerebral microhemorrhages: mechanisms, consequences, and prevention. Am J Physiol Heart Circ Physiol. 2017;312(6):H1128-h1143.
24. Kato H, et al. Silent cerebral microbleeds on T2*-weighted MRI: correlation with stroke subtype, stroke recurrence, and leukoaraiosis. Stroke. 2002;33(6):1536–40.
25. Toth P, et al. Functional vascular contributions to cognitive impairment and dementia: mechanisms and consequences of cerebral autoregulatory dysfunction, endothelial impairment, and neurovascular uncoupling in aging. Am J Physiol Heart Circ Physiol. 2017;312(1):H1–20.
26. Springo Z, et al. Aging impairs myogenic adaptation to pulsatile pressure in mouse cerebral arteries. J Cereb Blood Flow Metab. 2015;35(4):527–30.
27. Toth P, et al. IGF-1 deficiency impairs cerebral myogenic autoregulation in hypertensive mice. J Cereb Blood Flow Metab. 2014;34(12):1887–97.
28. Toth P, et al. Age-related autoregulatory dysfunction and cerebromicrovascular injury in mice with angiotensin II-induced hypertension. J Cereb Blood Flow Metab. 2013;33(11):1732–42.
29. Toth P, et al. Role of 20-HETE, TRPC channels, and BKCa in dysregulation of pressure-induced Ca2+ signaling and myogenic constriction of cerebral arteries in aged hypertensive mice. Am J Physiol Heart Circ Physiol. 2013;305(12):H1698–708.
30 De Reuck JL, et al. Microbleeds in postmortem brains of patients with Alzheimer disease: a T2*-weighted gradient-echo 7.0 T magnetic resonance imaging study. Alzheimer Dis Assoc Disord. 2013;27(2):162–7.
31. Freeze WM, et al. Blood-brain barrier leakage and microvascular lesions in cerebral amyloid angiopathy. Stroke. 2019;50(2):328–35.
32. Ni J, et al. Cortical localization of microbleeds in cerebral amyloid angiopathy: an ultra high-field 7T MRI study. J Alzheimers Dis. 2015;43(4):1325–30.
33. Park JH, et al. Pathogenesis of cerebral microbleeds: in vivo imaging of amyloid and subcortical ischemic small vessel disease in 226 individuals with cognitive impairment. Ann Neurol. 2013;73(5):584–93.
34. van Veluw SJ, et al. Different microvascular alterations underlie microbleeds and microinfarcts. Ann Neurol. 2019;86(2):279–92.
35. Graff-Radford J, et al. Cerebral amyloid angiopathy burden and cerebral microbleeds: Pathological evidence for distinct phenotypes. J Alzheimers Dis. 2021;81(1):113–22.
36. Rotta J, et al. Detection of cerebral microbleeds with venous connection at 7-Tesla MRI. Neurology. 2021;96(16):e2048–57.
37. Shaaban CE, et al. In vivo imaging of venous side cerebral small-vessel disease in older adults: An MRI Method at 7T. AJNR Am J Neuroradiol. 2017;38(10):1923–8.
38. Zhang R, et al. The relationship between deep medullary veins score and the severity and distribution of intracranial microbleeds. Neuroimage Clin. 2019;23:101830.
39. Dinc N, et al. Thrombosis of the straight sinus and microbleedings due to deep seated arteriovenous fistula - hemodynamic changes, cognitive impairment and improvement after microsurgery. A technical report. J Clin Neurosci. 2019;68:317–21.
40. Ungvari Z, et al. Repeated Valsalva maneuvers promote symptomatic manifestations of cerebral microhemorrhages: implications for the pathogenesis of vascular cognitive impairment in older adults. Geroscience. 2018;40(5–6):485–96.
41. Nyul-Toth A, et al. Cerebral venous congestion exacerbates cerebral microhemorrhages in mice. Geroscience. 2022;44(2):805–16.
42. Miller LR, et al. Increased susceptibility to cerebral microhemorrhages is associated with imaging signs of microvascular degeneration in the retina in an insulin-like growth factor 1 deficient mouse model of accelerated aging. Front Aging Neurosci. 2022;14:788296.
43. Tarantini S, et al. Insulin-like growth factor 1 deficiency exacerbates hypertension-induced cerebral

microhemorrhages in mice, mimicking the aging phenotype. Aging Cell. 2017;16(3):469–79.
44. Toth P, et al. Aging exacerbates hypertension-induced cerebral microhemorrhages in mice: role of resveratrol treatment in vasoprotection. Aging Cell. 2015;14(3):400–8.
45. Wakisaka Y, et al. Critical role for copper/zinc-superoxide dismutase in preventing spontaneous intracerebral hemorrhage during acute and chronic hypertension in mice. Stroke. 2010;41(4):790–7.
46. Wakisaka Y, et al. Spontaneous intracerebral hemorrhage during acute and chronic hypertension in mice. J Cereb Blood Flow Metab. 2010;30(1):56–69.
47. Wakisaka Y, et al. Oxidative stress through activation of NAD(P)H oxidase in hypertensive mice with spontaneous intracranial hemorrhage. J Cereb Blood Flow Metab. 2008;28(6):1175–85.
48. Braun DJ, et al. Genetic knockout of myosin light chain kinase (MLCK210) prevents cerebral microhemorrhages and attenuates neuroinflammation in a mouse model of vascular cognitive impairment and dementia. Geroscience. 2019;41(5):671–9.
49. Fisher M, et al. Therapeutic modulation of cerebral microhemorrhage in a mouse model of cerebral amyloid angiopathy. Stroke. 2011;42(11):3300–3.
50. Hur J, et al. Cerebrovascular beta-amyloid deposition and associated microhemorrhages in a Tg2576 Alzheimer mouse model are reduced with a DHA-enriched diet. FASEB J. 2018;32(9):4972–83.
51. Nyul-Toth A, et al. Increases in hypertension-induced cerebral microhemorrhages exacerbate gait dysfunction in a mouse model of Alzheimer's disease. Geroscience. 2020;42(6):1685–98.
52. Nishimura N, et al. Targeted insult to subsurface cortical blood vessels using ultrashort laser pulses: three models of stroke. Nat Methods. 2006;3(2):99–108.
53. Nyul-Toth A, et al. Demonstration of age-related blood-brain barrier disruption and cerebromicrovascular rarefaction in mice by longitudinal intravital two-photon microscopy and optical coherence tomography. Am J Physiol Heart Circ Physiol. 2021;320(4):H1370–92.
54. Shih AY, et al. Two-photon microscopy as a tool to study blood flow and neurovascular coupling in the rodent brain. J Cereb Blood Flow Metab. 2012;32(7):1277–309.
55. Ahn SJ, et al. Diverse inflammatory response after cerebral microbleeds includes coordinated microglial migration and proliferation. Stroke. 2018;49(7):1719–26.
56. Delekate A, et al. Metabotropic P2Y1 receptor signalling mediates astrocytic hyperactivity in vivo in an Alzheimer's disease mouse model. Nat Commun. 2014;5:5422.
57. Martín R, et al. Circuit-specific signaling in astrocyte-neuron networks in basal ganglia pathways. Science. 2015;349(6249):730–4.
58. Morquette P, et al. An astrocyte-dependent mechanism for neuronal rhythmogenesis. Nat Neurosci. 2015;18(6):844–54.
59. Nimmerjahn A, et al. Sulforhodamine 101 as a specific marker of astroglia in the neocortex in vivo. Nat Methods. 2004;1(1):31–7.
60. Tarantini S, et al. Effect of genetic depletion of MMP-9 on neurological manifestations of hypertension-induced intracerebral hemorrhages in aged mice. Geroscience. 2021;43(5):2611–9.
61. Pétrault M, et al. Cerebral microbleeds: beyond the macroscope. Int J Stroke. 2019;14(5):468–75.
62. Charidimou A, Jäger HR, Werring DJ. Cerebral microbleed detection and mapping: principles, methodological aspects and rationale in vascular dementia. Exp Gerontol. 2012;47(11):843–52.
63 Golino P, et al. Local platelet activation causes vasoconstriction of large epicardial canine coronary arteries in vivo. Thromboxane A2 and serotonin are possible mediators. Circulation. 1989;79(1):154–66.
64. Bell RD, et al. Pericytes control key neurovascular functions and neuronal phenotype in the adult brain and during brain aging. Neuron. 2010;68(3):409–27.
65. Hartmann DA, Coelho-Santos V, Shih AY. Pericyte control of blood flow across microvascular zones in the central nervous system. Annu Rev Physiol. 2022;84:331–54.
66. Hibbs E, Love S, Miners JS. Pericyte contractile responses to endothelin-1 and abeta peptides: assessment by electrical impedance assay. Front Cell Neurosci. 2021;15:723953.
67. Hirunpattarasilp C, et al. Hyperoxia evokes pericyte-mediated capillary constriction. J Cereb Blood Flow Metab. 2022;42(11):2032–47.
68. Hirunpattarasilp C, et al. SARS-CoV-2 triggers pericyte-mediated cerebral capillary constriction. Brain. 2023;146(2):727–38.
69. Liu Y, et al. 20-HETE-promoted cerebral blood flow autoregulation is associated with enhanced pericyte contractility. Prostaglandins Other Lipid Mediat. 2021;154:106548.
70. Levit A, Hachinski V, Whitehead SN. Neurovascular unit dysregulation, white matter disease, and executive dysfunction: the shared triad of vascular cognitive impairment and Alzheimer disease. Geroscience. 2020;42(2):445–65.
71. Tarantini S, et al. Impaired neurovascular coupling in aging and Alzheimer's disease: contribution of astrocyte dysfunction and endothelial impairment to cognitive decline. Exp Gerontol. 2017;94:52–8.
72. Pekny M, Pekna M. Astrocyte reactivity and reactive astrogliosis: costs and benefits. Physiol Rev. 2014;94(4):1077–98.
73. Bagi Z, et al. Vasodilator dysfunction and oligodendrocyte dysmaturation in aging white matter. Ann Neurol. 2018;83(1):142–52.
74. Ungvari Z, et al. Endothelial dysfunction and angiogenesis impairment in the ageing vasculature. Nat Rev Cardiol. 2018;15(9):555–65.
75. Rajani RM, Williams A. Endothelial cell-oligodendrocyte interactions in small vessel disease and aging. Clin Sci (Lond). 2017;131(5):369–79.
76. Manukjan N, et al. A systematic review of WNT signaling in endothelial cell oligodendrocyte interactions: potential relevance to cerebral small vessel disease. Cells. 2020;9(6):1545.
77. Dimovasili C, et al. Aging compromises oligodendrocyte precursor cell maturation and efficient remyelination in the monkey brain. Geroscience. 2023;45(1):249–64.

78. Skaper SD. Oligodendrocyte precursor cells as a therapeutic target for demyelinating diseases. Prog Brain Res. 2019;245:119–44.
79. Chojdak-Lukasiewicz J, et al. Cerebral small vessel disease: a review. Adv Clin Exp Med. 2021;30(3):349–56.
80. Jellinger KA. Alzheimer disease and cerebrovascular pathology: an update. J Neural Transm (Vienna). 2002;109(5–6):813–36.
81. Vemuri P, et al. White matter abnormalities are key components of cerebrovascular disease impacting cognitive decline. Brain Commun. 2021;3(2):fcab076.
82. Zhou H, Tang Y, Yuan Z. White matter asymmetries in patients with cerebral small vessel disease. J Integr Neurosci. 2018;17(2):159–67.
83. Sekhon LH, et al. Chronic cerebral hypoperfusion and impaired neuronal function in rats. Stroke. 1994;25(5):1022–7.
84. Lee C, et al. Imaging cerebral blood flow in the cognitively normal aging brain with arterial spin labeling: implications for imaging of neurodegenerative disease. J Neuroimaging. 2009;19(4):344–52.
85. Shibasaki H. Human brain mapping: hemodynamic response and electrophysiology. Clin Neurophysiol. 2008;119(4):731–43.